Chapter 4

Measuring redshifted 21 cm signal using Combine lense estimator

[*] In chapter 3, we discussed that the strong lensing by individual galaxy clusters enhances the H I power spectrum at the scale of the cluster or lower. The effect of strong lensing by individual clusters is effective only in a limited region of the sky and as discussed, gives rise to large sample variance. In this Chapter, we construct an unbiased power spectrum estimator with the lensed visibilities and explore the detection criteria of redshifted 21 cm signal from the post reionization era using strong gravitational lensing by the combination of signals from many cluster lenses. The estimator developed here is based on the visibility based power spectrum discussed in Choudhuri et al. (2014). Here we assume that the lensing potential is well known and explore the uncertainties in the measurement of the power spectrum only arising from sample variance and instrumental errors.

---

[*] A part of the work presented in this chapter was originally published in the paper titled " Combined lensed estimator to probe the post reionization H I power spectrum" by (Arora and Dutta, 2021)

4.1 Combined Lensed Estimator

4.1.1 Effect of Strong Lensing

Arora and Dutta (2020) has explored the modification of the 21 cm power spectrum from a strongly lensed region. We can write the brightness temperature fluctuation of 21 cm emission originating from redshift z_s through a strong lens at redshift z_L as

$$\delta I_L(\vec{\theta}, z_s, z_L) = \int d\vec{\theta}' \delta I(\vec{\theta}', z_s)\, G_L(\vec{\theta} - \vec{\theta}', z_s, z_L), \tag{4.1}$$

where $G_L(\vec{\theta} - \vec{\theta}', z_s, z_L)$ is the point spread function of the gravitational lens. For a gravitationally lensed signal, radio interferometers measure the visibility function $V(\vec{U}, z_s, z_L)$ as

$$V(\vec{U}, z_s, z_L) = S_L(\vec{U}, z_s, z_L) V_s(\vec{U}, z_s) + N(\vec{U}). \tag{4.2}$$

Here S_L is the lens sampling function and is the Fourier transform of G_L. The quantity $N(\vec{U})$ denotes the complex system noise at each baseline. The quantity $V_s(\vec{U}, z_s)$ is related to $\Delta\tilde{I}(\vec{U}, z_s)$ as

$$V_s(\vec{U}) = \int d\vec{U}\, \tilde{a}(\vec{U} - \vec{U}') \Delta\tilde{I}(\vec{U}) \tag{4.3}$$

where $\tilde{a}(\vec{U})$ is the antenna beam pattern. We have not explicitly written the redshift dependence henceforth. This quantity V_s represents the visibility in the absence of any lens and is measured by an interferometer with no noise. In practice, the antenna beam pattern can be complex. However, for most of the interferometers, a Gaussian function approximates the antenna beam (Choudhuri et al., 2014). In this chapter, we assume the antenna beam pattern to have the following form and use it henceforth.

$$\tilde{a}(\vec{U}) = \pi\theta_0^2 \exp\left[-\pi^2\theta_0^2 U^2\right], \tag{4.4}$$

where θ_0 defines the field of view of observation. We define

$$V_{2S}(\vec{U},\Delta\vec{U}) = \langle V_S(\vec{U})V_S^*(\vec{U}+\Delta\vec{U})\rangle. \tag{4.5}$$

Using eqn (4.3) and eqn (2.12) we can write above as

$$V_{2S}(\vec{U},\Delta\vec{U}) = \left(\frac{\partial B}{\partial T}\right)^2 \int d\vec{U}\,\tilde{a}(\vec{U}-\vec{U}')\,\tilde{a}^*(\vec{U}+\Delta\vec{U}-\vec{U}')\,C_l. \tag{4.6}$$

In the limit $\mid \Delta\vec{U} \mid << 1/\theta_0$, we may write above as

$$V_{2S}(\vec{U},\Delta\vec{U}) = V_{20}\,D(|\Delta\vec{U}|)\,C_l \tag{4.7}$$

where $D(\Delta\vec{U}) = \exp\left[-\pi^2\theta_0^2 \mid \vec{U}-\vec{U}' \mid^2\right]$ and $V_{20} = \frac{\pi\theta_0^2}{2}\left(\frac{\partial B}{\partial T}\right)^2$.

4.1.2 Power Spectrum Estimator

Interferometers sample visibilities at discrete baseline positions given by instantaneous projected separation of antenna pairs in the sky plane in units of observed wavelengths. We denote one sample of the visibility function measured at a baseline $\vec{U}$ through a particular gravitational lens as V_i. Using eqn (4.2) we can write V_i in terms of the lens sampling function S_{Li} at that baseline for the same lens, V_{Si}, and system noise N_i as

$$V_i = S_{Li}V_{Si} + N_i. \tag{4.8}$$

Arora and Dutta (2020) have shown the effect of lensing by a single cluster and demonstrated the increase in the observed signal in the presence of lensing. However, they do not discuss an unbiased estimator of the 21 cm power spectrum. Moreover, one limitation in their method is that strong lensing enhances the signal only near the caustics making the enhanced signal sample variance limited. They show that the lensing sampling function enhances the visibility correlation only when its modulus is above unity and such baseline positions for a single gravitational lens can be limited. Since the brightness temperatures are assumed to be the homogeneous and isotropic, observation of the specific intensity fluctuation at the different directions in the sky at the same redshift z_s can be used to probe the statistical nature of the signal V_S at that redshift. Hence, we may combine estimates of the power spectrum by several galaxy clusters to effectively enhance the sampling of the baseline plane. In this approach, we invert the effect of lensing to estimate the power spectrum of sky brightness distribution unbiasedly. Here we assume that the lensing sampling function is known from an earlier study to considerable accuracy.

We construct the angular power spectrum estimator in the following way[†]. We first grid the baseline plane with grid size $\sim 1/\theta_0$. We collect visibilities from one lens in the sampled baseline grids. The mean of the angular power spectrum and its uncertainties are then estimated in each grid. We define, for each grid,

$$E_L(g) = \frac{1}{V_{20}P} \sum_{i,j} w_{ij} V_i V_j^* \tag{4.9}$$

where the summations are over all the measured visibilities in a grid. Here D_{ij} is the function $D(\Delta U)$ defined in eqn (4.7) with ΔU being the magnitude of the separation of i^{th} and j^{th} baselines. The weight factor w_{ij} has the form $w_{ij} = \Delta_{ij} k_{ij}$, where $\Delta_{ij} = (1 - \delta_{ij})$, δ_{ij} is the Kronecker delta and k_{ij} is chosen to enhance the signal to noise of the estimator. Here, we choose $k_{ij} = (S_{Li} S^*_{Lj})^{-1}$ and P is $Trace[P_{ij}]$ when $P_{ij} = \sum_k \Delta_{ik} D_{kj}$.

It is to be noted that, in a typical interferometer, the noise at each baseline is expected to be higher than the sky signal at that baseline. Hence, if we consider the visibility correlation between the same baseline, the noise term always dominates and gives rise to a bias in the estimator. The term Δ_{ij} ensures that the same baseline correlations are not taken in $E_L(g)$. Noise in a typical interferometer is also not correlated across the baselines. Hence, for an

---

[†] This is a modified version of the estimator discussed in Choudhuri et al. (2014)

interferometer, with per visibility mean square system noise as σ_N^2, $\langle N_i N_j^* \rangle = 2\sigma_N^2 \delta_{ij}$. In presence of enough visibility measurements in the grid g and absence of foreground, the quantities $E_L(g)$ gives an unbiased estimate of the angular power spectrum C_{l_g} in the grid g defined by $\vec{U}_g = (u_g, v_g)$ as $u_g = \sum_i P_{ii} u_i / P, \;\; v_g = \sum_i P_{ii} v_i / P$.

The baseline grid with $\vec{U}_g = (u_g, v_g)$ correspond to the multipole $l_g = 2\pi\sqrt{u_g^2 + v_g^2}$. There is only one estimate of the angular power spectrum in a given grid. Uncertainty in this estimate, in the same grid is given as

$$\sigma_g^2 = \frac{\left[C_{l_g}^2 \sum_{i,j} P_{ij} P_{ji} + \eta C_{l_g} \sum_{i,j} P_{ij} \Delta_{ji} k_{ii} + \eta^2 \sum_{i,j} k_{ii} \Delta_{ij} k_{jj} \right]}{P^2}, \tag{4.10}$$

where $\eta = \frac{2\sigma_N^2}{V_{20}}$. Note that, with the choice of k_{ij} here, we have made the estimates of C_l in the grids independent of the lensing sampling function. However, the uncertainties in the estimates in each grid depend on the grid itself.

If observations of the lensed redshifted 21 cm signal are done for directions of multiple cluster lenses, then we collect all estimates of C_{l_g} and σ_g^2 in the same grids in the baseline plane. For the grids where with contribution from more than one cluster lens we average over the estimates of C_{l_g} and quadrature average over the estimates of σ_g^2. The azimuthally averaged estimates of the angular power spectra C_l and its variance σ_l^2 in a bin representing angular multipole l can be written as

$$C_l = \sum_g C_{l_g} / N_G, \qquad \text{and} \quad \sigma_l^2 = \sum_g \sigma_{C_g}^2 / N_G^2, \tag{4.11}$$

where the summation is over the number of grids N_G in the annulus with estimates of C_{l_g} and the above measurements are at $l = \sum_g l_g / N_G$.

4.2 Implementation of the Estimator

The basic idea of the combined lens estimator and its variance is discussed in section 4.1.2. Here we discuss the implementation of the estimator through the following steps.

4.2.1 Calculation of S_L in the observed baseline positions

In this chapter, we assume that we are using gravitational lenses with sufficiently well-constrained lensing potential. Estimation of the lensing sampling function S_L from the projected potential of the lenses is discussed in Arora and Dutta (2020). We estimate the magnification function of the lenses from their known projected potential. For the cluster lenses, the extent of the lensing potentials is significantly large as compared to the observing wavelengths. Hence the magnification function of the lens can be approximated as the point spread function G_L (Loutsenko, 2018). We first estimate G_L in a grid in the sky plane. We choose the grid size based on the angular resolution of the telescope. Extend of the grid in the sky plane, over which G_L is calculated, is chosen such that the lens with the largest extent has unit magnification at the edge of the grid and beyond. While observing, an interferometer samples the visibility function at particular baseline positions given by the instantaneous projected separation of antenna pairs in the sky plane in terms of the wavelength of observation. The sampling of the visibility function in the baseline plane by a typical interferometer depends on its location, antenna configuration, declination of the source and observing time. For all the lenses we estimate the lensing sampling function in the observed baseline positions by calculating the non-uniform Fast Fourier Transform of G_L of the particular lens. If for a given lens, a particular baseline has $S_L < 1$, lensing enhances the noise in the angular power spectrum estimate. We choose a threshold value S_T for the modulus of lensing sampling function. We use measurements from a particular pointing in a grid only if $\mid S_L \mid > S_T$ in that grid for the pointing. We always choose $S_T \geq 1$, for every grid, to reduce noise enhancement by lensing. Note that this further changes the sampling of the baseline plane and hence the term “Lensing sampling function" is used for $S_L(\vec{U})$.

4.2.2 Gridding the observed lens visibilities

We construct a grid in the baseline plane. Since every interferometer can measure to a maximum baseline, we need to only grid the baseline plane to the maximum baseline U_M. Note that, in presence of the term $D(\mid \Delta\vec{U} \mid)$ in eqn (4.7), the visibility correlation V_{2S} drops rapidly as $\mid \Delta\vec{U} \mid$ increases beyond $1/\theta_0$. If the caustics of the lens have an extension smaller than the field of view of the telescope, the effective value of θ_0 may be taken as the extent of the caustics itself. We choose the grid-size of the baseline grids as $U_m = 1/(\pi\,\theta_0)$. This ensures that the visibility correlations contribute significantly to the measurements of the angular power spectrum in each grid. We label the visibility measurements based on the baseline grid and the lens. For a given lens, if the number of measurements of visibilities in a given grid N_b is rather less, an estimate of the angular power spectrum in that grid is not statistically significant. In fact, to estimate the power spectrum, we need at least two baselines in a given grid. We define a threshold number $N_T > 2$, such that we use a grid, only if $N_b > N_T$. The grids which have $N_b < N_T$ are discarded. We use the measurements in the rest of the grids for further analysis. Note that increasing both N_T and S_T decreases uncertainties in each grid. However, it also decreases the number of grids N_G in a given annulus. Hence, an optimum choice is to be made while deciding on S_T and N_T.

4.2.3 Estimates of C_l and its variance

Given a lens, we estimate the angular power spectrum in the grids where $N_b > N_T$ by directly using the estimator as given in eqn (4.9). We also calculate the value of l_g corresponding to the grid. An estimate of the variance in each of these grids is obtained using eqn (4.10). Estimation of the quantity σ_N will be discussed in the next section.

We collect contributions from all lenses for l_g, C_{l_g} and σ_g^2 in the baseline plane grids. We divide the baseline plane in azimuthal bins with their boundaries in logarithmic intervals. For each bin, we estimate the azimuthally average angular power spectrum and its uncertainty following the definition in eqn (4.11). This gives us a measurement of the 21 cm angular power spectra and its uncertainty as a function of the angular multipole.

4.3 Simulations and Results

In this section, we demonstrate the effectiveness of the angular power spectrum estimator defined above by using a fiducial model for the 21 cm angular power spectrum as discussed in section (2.5) and parametric models of known lenses from optical studies.

4.3.1 Lens Model

We have used the PIEMD Lens model as discussed in section (3.2.1) in order to implement Combine Lens Estimator we use the galaxy cluster from Abell Catalogue and use Dark matter halo components of them.

We consider the contributions from all the components of cluster lenses with $\theta_s > 10''$ for the calculations. Table 4.1 gives the lens parameters for 19 clusters from the Abell cluster catalogue. The clusters are arranged in increasing order of their redshifts. The lens models used here are obtained from the references given in the table, where they use lensed multiple images of background sources in optical wavelengths to model the cluster potential. For some of the clusters, a few parameters are not well constrained as of now, these are marked with a star '+' against their names. We also restrict to clusters with at least most of the parameters well constrained and not considered clusters with a large elliptic component. Fig (4.1) shows the critical curves for all the cluster lenses if they had been in the same direction in the sky. The source redshift is taken to be 1.5. This shows

Models	z_l	θ_{x0} ($''$)	θ_{y0} ($''$)	ε	χ ($^\circ$)	θ_a ($''$)	θ_s ($''$)	σ_v (km sec^{-1})	References
A1413	0.143	0	0	0.67	85.1	25.9	386.3	941	3
		0	0	0.71	65.0	0.02	48.6	334	
		13.2	-19.9	0.12	36.6	0.04	12.1	168	
A2204	0.152	0	0	0.54	134.6	4.9	366.5	556	3
A868	0.153	0	0	0	-66.5	26.0	364.5	1078	3
		-21.5	11.7	0.42	26.2	22.9	364.5	426	
A2218	0.171	3.1	20.8	0.04	38.0	19.4	198.4	697	3
		-16.9	-21.7	0.32	9.2	39.8	161	992	
		-0.5	0.1	0.46	52.4	1.7	12.7	506	
A1689	0.183	0.6	-8.9	0.21	91.8	32	477.5	1437	6
		-70.0	47.8	0.80	80.5	22.1	157.8	643	
A383	0.187	-0.3	0.5	0.15	123.7	88.3	309.6	1976	3
A209	0.200	0	0	0.57	43.0	14.7	293.7	630	1
A963	0.206	0	0	0.21	85.0	6.7	286.9	74	3
A773	0.217	0	0	0.62	-37.3	11.6	275.7	501	3
		0	24	0.47	-20.2	35.3	275.7	836	
		-119	6^+	0.42	-54.4^+	20.7	275.7	996	
A2219	0.228	0.1	0.2	0.65	32.9	20.4	265.5	854	3
		-39.2	-32	0.10	7.6	41.7	265.5	781	
		-22.9	4.5	0.00	0.0	2.1	265.5	328	
A267	0.230	0	0	0.6	-60.0	30.3	263.8	1060	1
A2667	0.230	0.1^+	-0.5^+	0.32	-44.1	21.8	342.4	1114	3
A2390	0.231	38.9	27.4	0.61	215.1	155.7	525.8	2038	3
		-0.9	-1.4	0.03^+	30.5	7.86	77.5	633	
		46.9	12.8	0.35	143.7	0.01	10.9	152	
A521	0.247	0	0	0.67	49.5	4.6	250.1	553	3
A1835	0.253	4.8	0.7	0.57	77.7	24.4	245.7	1219	3
A68	0.255	-1.5	0.2^+	0.53	125.9	21.5	302.7^+	908	2
		-48.4	63.2	0	0	15.9	329.8	757	
A611	0.288	0	0	0.37	-47.3	9.5	223.9	854	3
A2744	0.308	-4.9	2.7	0.28	65	45.8	213.8	1263	5
		-15.7	-17.2	0.61	43.3	9.3	213.8	134	
A370	0.375	0.1	34.9	0.1	89.4	17.8	281.8	1040	4
		-2.5	1.9	0.47	80.8	16.6	281.8	969	

Table 4.1: PIEMD model parameters of the projected lensing potential for clusters in our sample. Columns are having values of redshift, centre of the ellipsoid, ellipticity, orientation, core and cut radii, velocity dispersion of these mass components. The '+' against some of the parameters represents those having less than one-sigma significance. The models are taken from 1. Smith et al. (2005) 2. Richard et al. (2007) 3. Richard et al. (2010b) 4. Johnson et al. (2014) 5. Jauzac et al. (2015) 6. Bina et al. (2016)

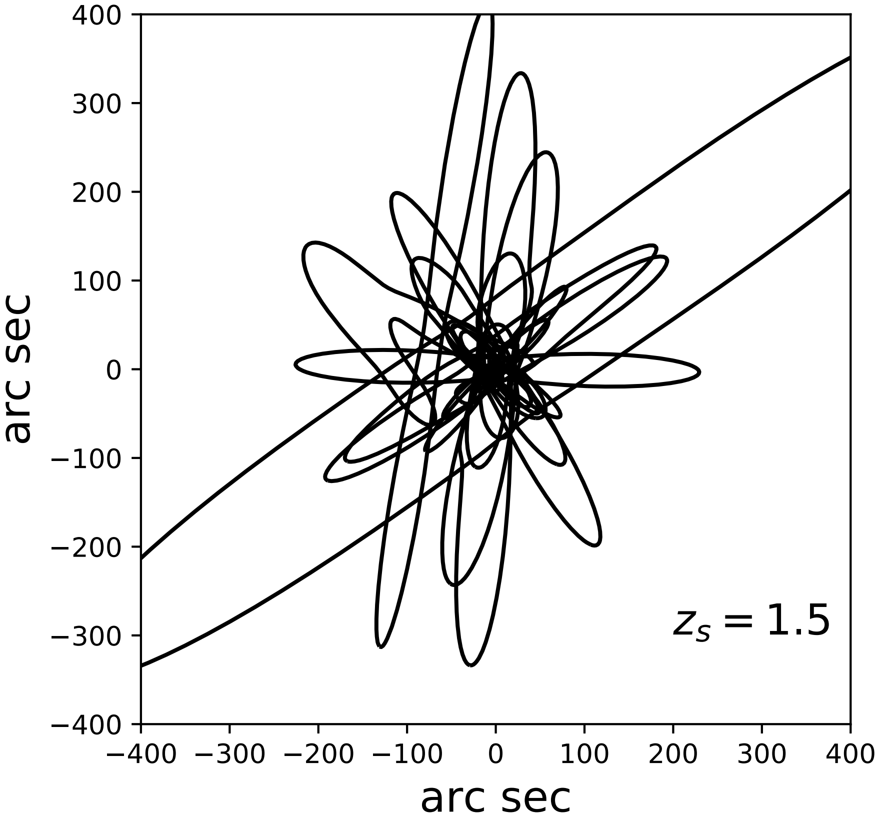

Figure 4.1: Central part of the critical curves for all the lens models given in Table 4.1 shown for a source redshift of 1.5.

that by using multiple lenses we can obtain magnification over a large fraction of the sky. We also notice that the sampling of the sky is better at smaller angular scales.

4.3.2 Results

In radio interferometric observations, noise in each observed visibility σ_N observed in a given frequency channel depends on the source equivalent flux density (SEFD) of the observing telescope, the integration time of observation $\Delta\tau$ and the width of the frequency channel over which the signal is integrated with frequency. If a signal remains correlated over a certain frequency range ν_c, then one can choose that as the width of the frequency channel of observation, provided the bandwidth smearing effect is not important. Assuming that the property of the signal does not change over nearby channels of width ν_c, we can estimate independent samples of the signal by including several channels to a total bandwidth of B_w. Then effectively,

$$\sigma_N^2 = \frac{[SEFD]^2}{\Delta\tau\sqrt{B_w \nu_c}}. \tag{4.12}$$

The observed interferometric signal we discuss here depends on the sky brightness distribution at the source redshift as well as the property of the gravitational lens. Bharadwaj and Ali (2005) has discussed how the 21 cm signal decorrelates with angular frequencies. They show that at different redshifts and angular multipoles, the bandwidth over which the signal remains correlated changes. Using their result, we find that the visibility correlation signal remains correlated for a frequency separation of 350 kHz, 400 kHz and 4.1 MHz at redshifts of $1.25, 1.5$ and 3.0 respectively at the angular multipole of 1000. Here, in addition, we need to investigate how the lensing sampling function changes with frequency. Note that, change in the lensing sampling function with frequency is expected to depend on the particular lens used. Fig 4.2 shows quantity $\langle S_L^*(\nu) S_L(\nu+\Delta\nu)\rangle / \langle | S_L^*(\nu) |^2\rangle$ as a

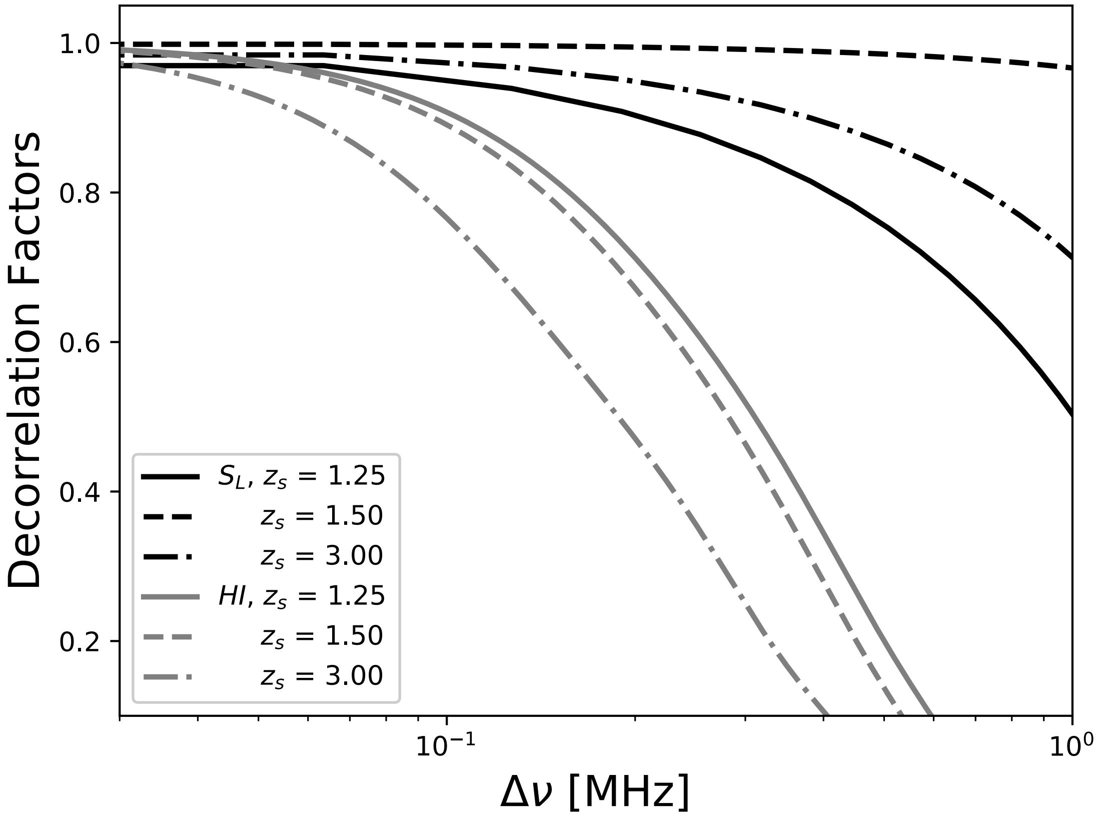

Figure 4.2: Figure showing how the lensing sampling function at the multipole of 1000 remains correlated with frequency. Here y-axis is in a relative scale with the value at $\Delta\nu$ set to unity. The black lines correspond to the lensing sampling function and the grey lines correspond to the H I signal.

function of frequency separation $\Delta\nu$ for these redshifts at the angular multipole of 1000 for the lens Abell 773. The de-correlation of the lensing sampling function is slower than that of the sky visibility correlation. Hence, we choose the de-correlation frequency of the sky visibility correlation as the value for ν_c. We shall mention any change in these parameters whenever necessary. We choose $N_T = 5$ for the estimations henceforth, which gives at least 10 baseline pairs within a grid. We also neglect the effect of foreground here, its effect will be discussed later.

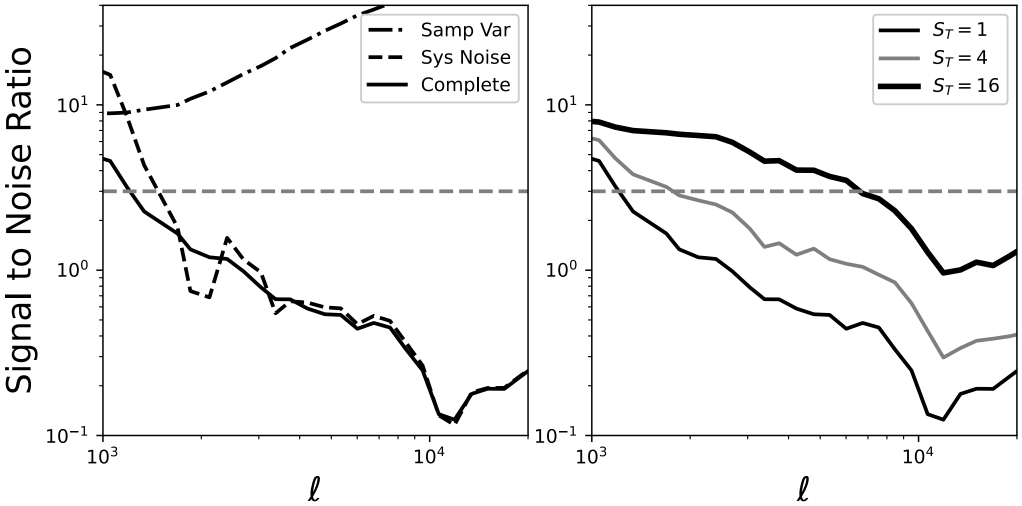

Figure 4.3: Signal to noise ratio (SNR) for the cluster Abell 773 for 250 hours observations with the uGMRT with a bandwidth of 16 MHz. Left panel: The black continuous line shows the signal to noise ratio for $S_T = 1$. The dashed line corresponds to the case when there is no effect of sample variance, whereas the dot-dashed line shows the SNR if instrumental noise is negligible. Right panel: Signal to noise ratio for different values of S_T. In both panels, the grey dashed line marks three-sigma confidence level.

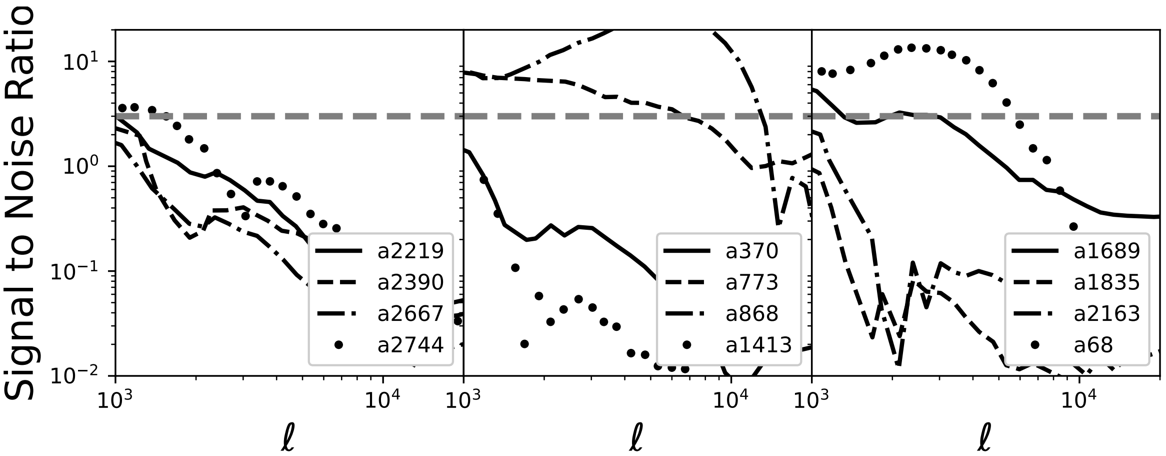

Figure 4.4: Signal to noise ratio for the best clusters in our sample for 250 hours observations with the uGMRT with a bandwidth of 16 MHz shown in three panels. The grey dashed line marks three-sigma confidence level.

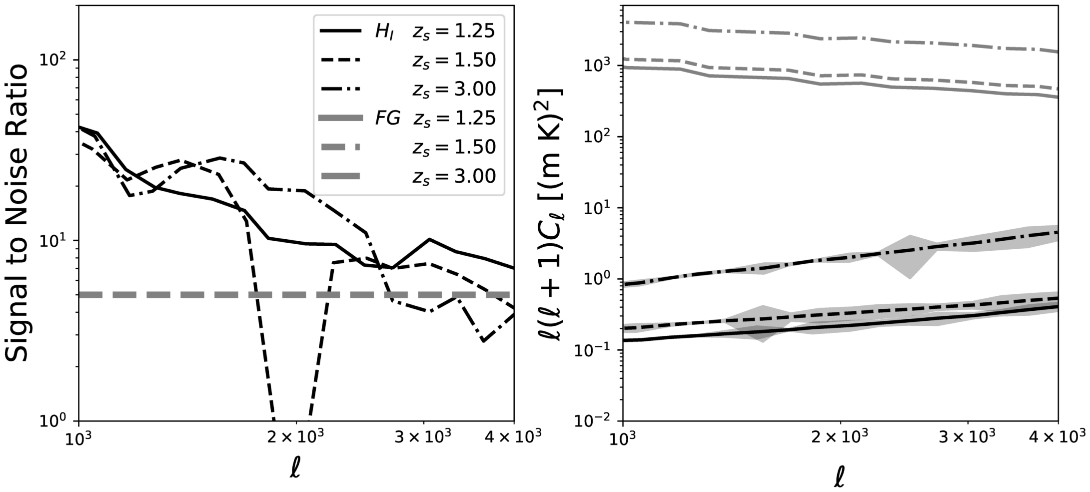

Figure 4.5: Left panel: Signal to Noise ratio combining eight best clusters in our sample for redshifts of 1.25, 1.5 and 3.0. Each case is for 16 MHz bandwidth uGMRT observation. For redshifts of 1.25 and 1.5 with the total observation hours for all eight clusters is 400 hours, for the redshift of 1.5 the observation time is 200 hours only. The grey line shows the five-sigma confidence level. Right panel: Angular power spectrum at redshifts z= 1.25, 1.5 and 3.0 and corresponding modified DGSE. The grey region shows the one-sigma error in the power spectrum estimates. Legends for different cases are shown in the left panel and is used identically for both the panels of this figure.

We first show the signal to noise ratio achievable with 250 hours of the uGMRT observations of 21 cm signal from a redshift of 1.5 for the cluster lens Abel 773 with a 16 MHz of bandwidth. This cluster is a rather nearby cluster at a redshift of 0.217. The left panel of Fig 4.3 show the contribution to signal to noise ratio arising if the system noise is negligible (dash-dot), sample variance is negligible (dashed) and if all the contributions to noise are present (solid). The grey dashed horizontal line indicates a signal to noise of three. All these curves are shown for $S_T = 1$. The right panel of the same figure demonstrate the variation of the signal to noise ratio as the threshold value S_T is increased. We observe that at a S_T of 16, the signal to noise ratio for the angular power spectrum for 250 hours of the uGMRT observation with a bandwidth of 16 MHz through the cluster lens Abel 773 is above three-sigma till an angular multipole of ~ 6000. We observe that the SNR is lower for the low angular multipoles as a result of the low number of samples, whereas reducing the system noise is more important to achieve higher SNR at the larger multipoles.

Clearly, with $S_T = 16$, we recover the H I signal significantly above the three-sigma confidence. We next use $S_T = 16$ to access the efficacy of the gravitational lenses for all the clusters in Table 4.1. Three panels of Fig 4.4 show signal to noise ratio for the clusters in our sample with values greater than unity anywhere for $l > 1000$. The horizontal thick black dashed line corresponds to the three-sigma significance. Clearly, most of the clusters are not very effective as a lens to enhance the H I signal significantly. The clusters, we find as good candidates for post-EoR H I signal enhancement are: Abell a68, Abell a868, Abell 1689, Abell 2219, Abell 2390, Abell 773, Abell 2744, Abell 370.

Fig 4.3 demonstrated that the signal to noise ratio in the H I signal improves with $S_T = 16$. Increasing S_T further reduces the number of grids available in the baseline plane and the sample variance error increase significantly. Subsequently, we used $S_T = 16$ for all the clusters in our sample to estimate the expected signal to noise ratio of lensed redshifted 21 cm signal from a redshift of 1.5. We found that nine of the clusters in our sample reduce the noise in the estimator to three-sigma significance for a bandwidth of 16 MHz and an observation time of 250 hours. However, for individual clusters, the range of angular multipoles over which we are sensitive is limited to certain angular multipole ranges. Next, we use the combined angular power spectrum estimates from all nine clusters. Since, while using multiple clusters we have estimates of the angular power spectra in enough grids in the baseline plane, we choose a value of $S_T = 32$.

The left panel of Fig 4.5 shows the signal to noise estimates of the lensed redshifted H I angular power spectra (black curves) at the redshifts of $1.25, 1.5$ and 3.0. We have chosen a bandwidth of 16 MHz and a total observation time of 400 hours here for the redshifts of 1.25 and 1.5. For the source redshift 3.0, we have a higher signal to noise and the plot shown here has a total observation time of 200 hours. The horizontal grey line indicates a signal to noise of 5. We find that 400 hours of observation is enough to observe lensed H I signal from the redshifts of $1.25, 1.5$ and 200 hours of observation is enough to observe the lensed H I signal from the redshift of 3.0 with five-sigma significance.

4.3.3 Effect of Foreground

The sky visibilities V_S in observation, at redshifted 21 cm frequencies, are dominated by the foreground diffused galactic synchrotron radiation from our galaxy. To observe the redshifted 21 cm signal one needs to model and subtract the diffused synchrotron foreground signal. Given that the amplitude of the foreground is much higher than the redshifted 21 cm signal, such observations require high dynamic range calibration of the observed visibilities (Datta et al., 2010; Kumar et al., 2020). The lensed 21 cm angular power spectrum estimator reduces the effective amplitude of this foreground and hence improves the calibration requirements. Note that in the presence of foreground, eqn (4.8) would have an additional term, V_{Fi} for the foreground, which is not enhanced by S_L. Since the foreground is not correlated with the 21 cm signal, the observed value of $E_L(g)$ in a given grid modifies to $C_{l_g} + C_{Fl_g} / \mid S_L(g) \mid^2$ approximately, where C_{Fl_g} is the angular power spectrum of the foreground and $S_L(g)$ is the lensing sampling function in the grid g. Since S_T is chosen to be 32 here, the effective contribution of the foreground in $E_L(g)$ decreases.

Black lines in the right panel of Fig 4.5 show the angular power spectra of the redshifted 21 cm signal at redshifts of $1.25, 1.5$ and 3.0. We also show the one-sigma errors with the grey bands for all three redshifts. The lens modified foreground angular power spectra corresponding to the H I signal from the same redshifts are shown with grey lines. Comparing with Fig 2.3, we observe that the foreground is suppressed approximately by a factor of 1000, however, is still significantly higher compared to the redshifted 21 cm signal. We believe this would help significantly to avoid excess bias and variance in the signal that may arise with a higher strength foreground through calibration errors.

4.4 Discussion and Conclusion

- In this chapter, we introduce a lensing based power spectrum estimator and calculate the uncertainties associated with these estimates. The estimator gives an unbiased estimate of the redshifted 21 cm power spectrum and suppresses the observational uncertainties which would be dominant if no lensing is used.

- We use strong lens models of a few clusters known from optical studies to investigate the efficacy of this estimator in enhancing the 21 cm angular power spectra from the post reionization era from redshifts of $1.25, 1.5$ and 3.0 using uGMRT baseline configuration.

- The highest redshift of a cluster in our sample is 0.375. We found that for 250 hours of uGMRT observation with a 16 MHz of bandwidth, three clusters in our sample, Abell 773, Abell 68 and Abell 868 which are at redshift of 0.217, 0.255 and 0.153

respectively, enhances the power spectra of the 21 cm emission from redshifts of 1.25, 1.5 and 3.0 statistically significantly.

- We find that these clusters effectively suppress the noise for angular multipoles $l < 6000$. It is found that a total of 400 hours of the uGMRT observation of these eight clusters, each with a bandwidth of 16 MHz, would let us estimate the 21 cm power spectra of H I at redshifts of 1.25 and 1.5 with five-sigma confidence up to an angular multipole of 4000. A similar sensitivity at a similar angular multipole range can be achieved with a total of 200 hours of observations of these clusters with the uGMRT for a redshift of 3.0.
- We find that for the parameters of the estimator chosen here, the effective foreground power spectra is reduced by a factor of 1000, which further reduces the bias and variance of the signal arising through the residual gain errors significantly.